SAND2019-4674J

Kinetic simulation of a low-pressure helium discharge with comparison to experimental measurements

Andrew Fierro, Ed Barnat, Chris Moore, Matthew Hopkins, Paul Clem

Sandia National Laboratories, Albuquerque NM 87185

E-mail: `andrew.s.fierro@ieee.org`

4 March 2019

Abstract. Modern computational validation efforts rely on comparison of known experimental quantities such as current, voltage, particle densities, and other plasma properties with the same values determined through simulation. A discrete photon approach for radiation transport was recently incorporated into a particle-in-cell (PIC)/Direct Simulation Monte Carlo (DSMC) code. As a result, spatially and temporally resolved synthetic spectra may be generated even for non-equilibrium plasmas. The generation of this synthetic spectra lends itself to potentially new validation opportunities. In this work, initial comparisons of synthetic spectra are made with experimentally gathered optical emission spectroscopy. A custom test apparatus was constructed that contains a 0.5 cm gap distance parallel plane discharge in ultra high purity helium gas (99.9999%) at a pressure of 75 torr. Plasma generation is initiated with the application of a fast rise-time, 100 ns full-width half maximum, 2.0 kV voltage pulse. Transient electrical diagnostics are captured along with time-resolved emission spectra. A one-dimensional simulation is run under the same conditions and compared against the experiment to determine if sufficient physics are included to model the discharge. To sync the current measurements from experiment and simulation, significant effort was undertaken to understand the kinetic scheme required to reproduce the observed features. Additionally, the role of the helium molecule excimer emission and atomic helium resonance emission on photocurrent from the cathode are studied to understand which effect dominates photo-feedback processes. Results indicate that during discharge development, atomic helium resonance emission dominates the photo-flux at the cathode even though it is strongly self-absorbed. A comparison between the experiment and simulation demonstrates that the simulation reproduces observed features in the experimental discharge current waveform. Furthermore, the synthesized spectra from the kinetic method produces more favorable agreement with the experimental data than a simple local thermodynamic equilibrium calculation and is a first step towards using spectra generated from a kinetic method in validation procedures. The results of this study produced a detailed compilation of important helium plasma chemistry reactions for simulating transient helium plasma discharges.

Submitted to: *Plasma Sources Sci. Technol.*

Sandia National Laboratories is a multimission laboratory managed and operated by National Technology & Engineering Solutions of Sandia, LLC, a wholly owned subsidiary of Honeywell International Inc., for the U.S. Department of Energy's National Nuclear Security Administration under contract DE-NA0003525.

1. Introduction

The verification and validation (V&V) of scientific codes is an important aspect in establishing confidence in the code's ability to model a given system. Given sufficient V&V and demonstration of model accuracy for key quanitities of interest, a model can be a predictive tool for design purposes. In recent years, as more simulation tools have been produced for the investigation of plasma physics, the need for V&V efforts has been accepted [1]. Verification is the process of ensuring the physics models implemented in code are producing the expected results. This could be in the form of comparision to analytic functions [2] if they are available. Unit tests [3] have also been shown to be useful in testing functionality of a code. Validation, in the simplest definition, compares experiment versus verified simulation capabilities and investigates if the model contains sufficient physics (or not) to simulate a given condition or range of parameters. Validation experiments are usually explicitly designed to be simple and well characterized to aide in modeling efforts [4, 5]. The idea of benchmarking codes is also a useful exercise that performs code-to-code comparisions, usually from separate research groups and developed independently. One such benchmark of codes using PIC with Monte Carlo Collision (MCC) procedures allows for comparision to a capactive discharge in helium gas [6]. Earlier work compared RF discharge simulations from twelve different codes using a variety of methods including fluid and kinetic approaches [7]. More recently, comparison of streamer formation in an axisymmetric configuration has been examined for six different simulation tools [8]. Alternatively, existing experimental results published in literature could serve as potential candidates for validation exercises if they are carefully documented. For example, the EDIPIC simulation code has been validated against electric field measurements obtained through laser diagnostics in a low pressure one-dimensional helium glow discharge for various drive voltages [9].

V&V is an on-going effort and as new physics models are implemented in a particular code, the verification and/or validation of the model should be investigated. The research plasma simulation code, Aleph, developed at Sandia National Laboratories is a massively parallel electrostatic kinetic code that utilizes particle-in-cell (PIC) techinques with the Direct Simulation Monte Carlo (DSMC) method for binary particle collisions. Physics models native to the Aleph code include electron-neutral collisions, charge exchange collisions, photon interactions, heavy-body interactions, and n-body reaction rates. It has been exhaustively verified previously [10, 11, 12, 13, 14, 15] and benchmarked [16, 17] with excellent agreement. The recent development and implementation of discrete tracking of photons into this kinetic code [18] has necessitated the inception of a new validation exercise, complementary to other methods, that will stress the new capability.

The discrete photon method has shown the possibility to recreate entire emission spectra with no assumption for either the electron energy distribution function (EEDF) or population of excited states. Optical emission spectroscopy (OES) is a common diagnostic to determine plasma characteristics such as species temperatures [19, 20] and electron densities through stark broadening [21]. The non-invasive nature of OES makes it an appealing target for validation and is a natural fit for validation of synthesized emission spectra from the discrete photon approach. In general, it is easy to capture optical emissions but it is not always clear what generates the photons and how the photons transport from the plasma. The discrete photon method is a great tool for bridging what is observed in experiment and what conditions generated that emission.

In an attempt to use synthetic spectra as an early validation exercise for radiation transport in plasma discharges, an experiment of a parallel plate plasma discharge in helium gas has been constructed with optical access for taking spectroscopic measurements. Additionally, time-resolved voltage measurements are collected and used for the anode voltage in the simulation. Discharge current measurements are used as a supplemental validation quantity and the sensitivity of the discharge current is analyzed as the cathode feedback mechanisms (e.g. photoemission and ion-induced secondary electron emission) are varied. A transient plasma is generated and used as the validation comparison as DC or RF discharges may not always be easy to simulate due to the unknown time scales for equilibrium operating conditions. Additionally, this configuration also demonstrates the ability of the kinetic code to produce non-equilibrium solutions. Informal validation is performed here by comparing discharge currents and spectral line intensities via time-resolved emission spectra from

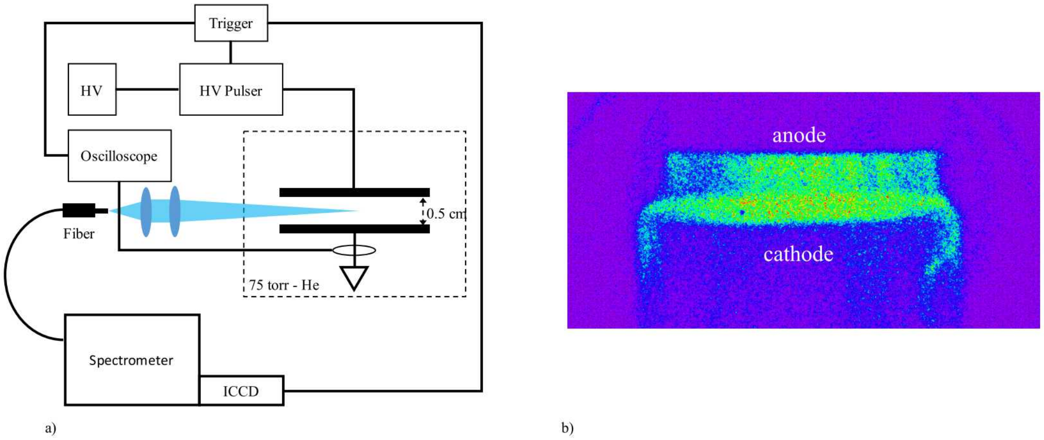

Figure 1. (a) Diagram of experimental setup consisting of the high voltage (HV) pulser, parallel plate gap, optical coupling system, and ICCD. (b) Representative image of a discharge event between the parallel plates at a pressure of 75 torr.

the experiment to that generated under the same conditions in the simulation. This work aims to utilize and compare experimental measurements with the simulations from the Aleph code such that detailed understanding of the discharge mechanics in a transient plasma is obtained. Furthermore, to obtain reasonable comparisons to experiment, a large number of chemistry reactions were necessary including atomic and molecular helium reactions. Thus, the chemistry set used here is considered a sufficient model to describe the current experiment and could be used as a basis for other models interested in simulating transient helium plasmas.

2. Experimental Setup

A simple experiment was constructed specifically to emulate a one-dimensional plasma environment to ease the PIC/DSMC computational costs that scale with dimensionality. Figure 1 gives an overview of the apparatus. A sealed vacuum chamber contains identical aluminum electrodes, each with a 2.54 cm diameter separated by a gap distance of 0.5 cm. A high voltage feedthrough allows access to the anode. The cathode is connected to the grounded chamber using a short lead allowing for electric current measurement with magnetic field sensors. To begin data acquisition, the entire system is initially pumped down to roughly 1 torr. An MKS mass flow controller allows the chamber to fill with helium gas at a rate of 180 SCCM. With the vacuum pump operating at full capacity and the flow rate set, a pressure of roughly 4.5 torr is obtained. This operating condition is held for several minutes to assist in removing contaminants from the discharge chamber. Lastly, the vacuum pump is closed off from the chamber and the pressure is brought to an operating pressure of 75 torr.

Plasma is generated via a DC high voltage power supply connected to a DEI PVX-4150 high voltage pulse generator for transient plasma formation. To reduce discharge jitter at a charging voltage of 2.0 kV, an Oriel mercury discharge lamp with strong emission in the UV is used to illuminate both the anode and cathode. It was noticed that without the application of the UV lamp, a large number of voltage applications did not result in breakdown. Electrical diagnostics include a voltage monitor provided by the DEI pulse generator and a Pearson current monitor (0.1 V/A sensitivity). The voltage pulse applied to the gap was nearly identical for every shot.

Light emission from the experiment is coupled to a fiber through a collimator lens system with focal length of approximately 7.5 cm. The fiber is then fed into a Princeton Instruments IsoPlane SCT-320 spectrograph (F/4.6). The spectrograph houses a triple grating turret, containing 2400 g/mm, 1200 g/mm, and 150 g/mm gratings. Only emission line intensity ratios are considered in this validation exercise, so line profiles are not too important. To capture a wide range of

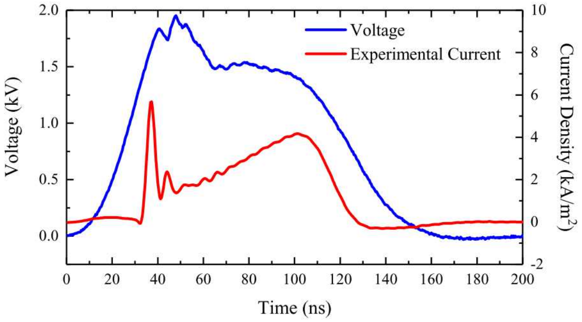

Figure 2. Time-corrected representative current density and voltage discharge waveforms for a 0.5 cm gap distance, 75 torr, helium gas pulsed discharge.

emission spectra in a single shot and avoid shot-to-shot variance, the 150 g/mm grating was utilized that has a 0.26227 nm/pixel dispersion. An Andor iStar DH334T camera with a 1024 x 1024 pixel matrix is used to capture the time-resolved emission spectra. For all measurements in this work, the camera gate was set to 10 ns with a gain of 4000 (x electrons/electron). Light emission from a white light source (Tungsten lamp operating at 3178 K) is used to calibrate the relative spectral efficiency of the optical system. To align the optical system, the fiber is back-illuminated using a low-power light source. The focal spot (radius approximately 500 micron) is oriented so that is visible on the cathode. The alignment system is linearly translated perpendicular to the cathode such that the light is no longer visible. A final height adjustment is made to set the center of the focal spot about 500 microns above the cathode.

A Tektronix 1 GHz oscilloscope, 4 Gigasamples/second, is used to capture the electrical signals. A common trigger pulse is used for the entire system and with the cable delays calculated, the camera gate and current waveforms are time-shifted to the measured voltage pulse. It is expected that the uncertainty in the timing is less than 5 ns. To capture time-resolved emission spectra, the trigger pulse to the ICCD camera was delayed further into the applied voltage pulse. It is noted that even under breakdown conditions the time from voltage application to current rise varied from from shot to shot. As a result, a series of shots was taken at each camera delay to reconstruct the spectra observed from a breakdown event that occured at similar times.

A representative open-shutter image of the plasma discharge is shown in Figure 1b. Time-corrected voltage and current density waveforms from a single shot are given in Figure 2. The actual conduction area of the electrodes is unclear as the plasma does not form uniformly across the gap. As a result, an electrode radius of smaller than the nominal radius is assumed for comparisons with simulation. This assumption is based upon the high-speed imaging (Figure 1b) that indicates some of the electrodes are not fully covered with plasma and that a brighter channel occurs in the center of the electrodes. The plasma also is observed to hug the lower portion of the cathode. However, it is assumed that this portion of the conduction current is negligible compared to directly between the anode and cathode beecause the light intensity is lower in this region.

3. Model Description and Setup

The simulation tool used here is a code developed at Sandia National Laboratories named Aleph. It is a massively parallel simulation tool utilizing the Message Passing Interface (MPI) framework and is used for mostly low-temperature plasma simulations operating in vacuum, to millitorr, and even more recently up to atmospheric pressure. Computational particle counts may easily exceed several billion, especially in relatively large domains (millimeter to centimeter sized geometries). Performance studies have shown acceptable scaling up to approximately 100,000 CPU cores. Electric field calculations are done electrostatically by solving Poisson's equation including space charge. Collective charged particle forces are handled with the PIC method [22]. The DSMC method [23] handles binary particle-particle or particle-photon interactions. More details of Aleph's PIC/DSMC scheme are provided elsewhere [24].

Aleph has been extensively verified, benchmarked, and even validated for some applications such as ion sheaths [33, 34]. With the inclusion of photonic mechanisms into this code, the need for new validation arises. The photon model is described in literature elsewhere [18, 2] and thus is only briefly described here. To generate a photon with wavelength λ, first an excited state, A^* is generated via an electron collision with species A

$$e^- + A \rightarrow e^- + A^*, \tag{1}$$

The rate of this reaction is a function of density of species A (A is allowed to be any species modeled in the system, e.g., neutrals, other excited states, ions), the relative velocity between the electron and A, v_{rel}, and the energy dependent cross section for the excitation, $\sigma(v_{rel})$. The excited species, A^*, is then allowed to decay in the simulation using the lifetime of the excited state, $\tau_{21} = 1/A_{21}$ where A_{21} is the Einstein coefficient for spontaneous emission. To determine if an emission

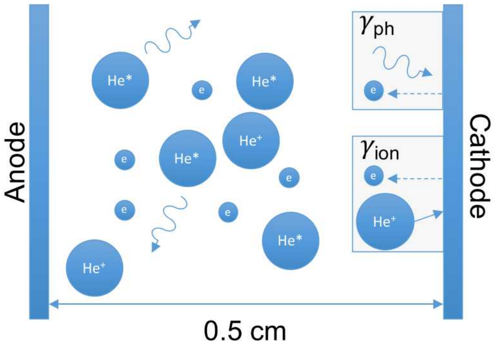

Figure 3. One-dimensional simulation model diagram. The feedback mechanisms at the cathode included in the simulation are secondary emission of electrons due to ion impact, γ_{ion}, and photoemission of electrons, γ_{ph}.

Table 1. Included binary reactions with the ground state (1^1S) that are included with cross section data. Unless noted, isotropic scattering is used for post-collision scattering angles.

	Reaction	Threshold Energy (eV)
	Elastic	
1^a	$e^- + 1^1S$	—
	Ionization	
2	$e^- + 1^1S \rightarrow 2e^- + He^+$	24.59
	Dipole-allowed excitation	
3	$e^- + 1^1S \rightarrow e^- + 2^1P$	21.22
4^b	$e^- + 1^1S \rightarrow e^- + 3^1P$	23.08
5	$e^- + 1^1S \rightarrow e^- + 4^1P$	23.74
	Dipole-forbidden excitation	
6	$e^- + 1^1S \rightarrow e^- + 2^1S$	20.61
7	$e^- + 1^1S \rightarrow e^- + 3^1S$	22.91
8^b	$e^- + 1^1S \rightarrow e^- + 3^1D$	23.07
9	$e^- + 1^1S \rightarrow e^- + 4^1S$	23.67
10^b	$e^- + 1^1S \rightarrow e^- + 4^1D$	23.73
11	$e^- + 1^1S \rightarrow e^- + 4^1F$	23.74
	Spin-forbidden excitation	
12	$e^- + 1^1S \rightarrow e^- + 2^3S$	19.82
13	$e^- + 1^1S \rightarrow e^- + 2^3P$	20.96
14	$e^- + 1^1S \rightarrow e^- + 3^3S$	22.71
15^c	$e^- + 1^1S \rightarrow e^- + 3^3P$	23.01
16^c	$e^- + 1^1S \rightarrow e^- + 3^3D$	23.07
17	$e^- + 1^1S \rightarrow e^- + 4^3S$	23.59
18^c	$e^- + 1^1S \rightarrow e^- + 4^3P$	23.71
19^c	$e^- + 1^1S \rightarrow e^- + 4^3D$	23.74
20	$e^- + 1^1S \rightarrow e^- + 4^3F$	23.74
	Self-absorption	
21	$h\nu$ (21.22 eV) $+ 1^1S \rightarrow 2^1P$	21.22^d
22	$h\nu$ (23.08 eV) $+ 1^1S \rightarrow 3^1P$	23.08^d
23	$h\nu$ (23.74 eV) $+ 1^1S \rightarrow 4^1P$	23.74^d

[a] Anisotropic scattering included [25]
[b] Cross section multiplied by factor 1.3
[c] Cross section multiplied by factor 0.3
[d] Indicates energy where the peak cross section is observed

event occurs, a uniform random number between 0 and 1, R, is drawn. If,

$$R < 1 - e^{-\Delta t/\tau_{21}} \tag{2}$$

with Δt the simulation timestep, then a photon is emitted with a wavelength, λ, such that $\lambda = \frac{h_p c}{E_{21}}$ where h_p is Planck's constant, c is the speed of light, and E_{21} is the energy difference between states A^* and A. The photon velocity vector is chosen from an isotropic distribution. Photons are then stepped through the simulation identically to other particles. A distribution of wavelengths for a single transition corresponding to a Voigt profile are generated in the simulation to emulate natural and Doppler line broadening mechanisms [18]. These result in vary narrow full width half maximum (FWHM) line widths (sub-nanometer) as compared to experimental observations but are important for including self-absorption mechanisms. To generate emission spectra from the simulation, a histogram of wavelengths for photons that exist in the simulation domain at a given sample time is computed. To emulate the finite integration time of the ICCD camera, numerous sample times are summed for a single histogram.

To compare experimental results and those generated via the photon model, a one-dimensional simulation is built to match the conditions of the experiment (Figure 3). Dirichlet boundary conditions are used for both the anode and cathode. The cathode is held at a constant 0 V potential. The anode, however, is provided a time-varying voltage pulse that was captured on the oscilloscope from the DEI high voltage pulse generator (see Figure 2). All charged particles are allowed to flux out of the simulation boundaries. Secondary emission of electrons from the cathode due to positive helium ion impact occurs with a fixed yield, γ_{ion}. In this model, photons with wavelengths longer than 120 nm do not interact with the background gas or electrodes. However, photons with a shorter wavelength cause photoemission of electrons from the cathode with a fixed quantum yield, γ_{ph}.

The binary collision method relies on accurate data for electron-impact cross sections. For electron-neutral elastic scattering, the cross section available from the Biagi database was used [35]. Electron-impact cross sections for excitation and ionization of the helium gas are tabulated from theoretical data provided in literature [36]. Table 1 shows the ground-state reactions included in the model. Reactions with excited states are also included but have virtually no effect as their densities are much lower than that of the ground-state with this model in these discharge conditions. The cross sections for dipole allowed, dipole forbidden, and spin forbidden have a reported error of 10%-30%, 10%-30%, and greater than 30%, respectively. To assist in reproducing the emission spectra more correctly, only the cross sections which result in emission that could be compared to experiment were modified as noted in the table. It should be noted that by kinetically simulating the photons, comparison between simulated and experimental emission spectra could be a viable method of accurately validating existing cross sections. But, other parameters in the simulation must be quantified for this method to be applicable. A calculation of Townsend's first ionization coefficient using the electron-neutral cross sections described above was compared against experimental results. Figure 4 demonstrates the comparison over the E/n (E = electric field, n = neutral background gas density)

Table 2. Included rate reactions not defined by a cross section. Reactions evaluated at a gas temperature, T_g of 300 K and electron temperature, T_e of 1 eV (∼11600 K).

	Reaction	Forward Rate (m^3/s or m^6/s)	Reverse Rate (m^3/s)	Reference
	l-change			
1	$1^1S + 3^3P \leftrightarrow 1^1S + 3^3D$	5.89×10^{-20}	1.45×10^{-18}	[26, 27]
2	$1^1S + 3^1P \leftrightarrow 1^1S + 3^1D$	3.16×10^{-16}	3.18×10^{-16}	[26, 27]
3	$1^1S + 4^3P \leftrightarrow 1^1S + 4^3S$	6.23×10^{-19}	2.52×10^{-21}	[26, 28]
4	$1^1S + 4^3D \leftrightarrow 1^1S + 4^3P$	5.05×10^{-17}	1.02×10^{-17}	[26, 28]
5	$1^1S + 4^3D \leftrightarrow 1^1S + 4^3S$	1.30×10^{-17}	1.07×10^{-22}	[26, 28]
6	$1^1S + 4^1D \leftrightarrow 1^1S + 4^1S$	5.29×10^{-18}	9.24×10^{-20}	[26, 28]
	Associative ionization			
7	$1^1S + 3^1P \rightarrow He_2^+ + e^-$	1.31×10^{-17}	—	[26]
8	$1^1S + 3^1D \rightarrow He_2^+ + e^-$	1.96×10^{-17}	—	[26]
9	$1^1S + 3^3S \rightarrow He_2^+ + e^-$	3.40×10^{-17}	—	[26]
10	$1^1S + 3^3P \rightarrow He_2^+ + e^-$	2.90×10^{-17}	—	[26]
11	$1^1S + 3^3D \rightarrow He_2^+ + e^-$	3.60×10^{-17}	—	[26]
12	$1^1S + 4^1S \rightarrow He_2^+ + e^-$	2.48×10^{-16}	—	[26]
13	$1^1S + 4^1P \rightarrow He_2^+ + e^-$	1.70×10^{-16}	—	[26]
14	$1^1S + 4^1D \rightarrow He_2^+ + e^-$	5.90×10^{-16}	—	[26]
15	$1^1S + 4^3S \rightarrow He_2^+ + e^-$	2.75×10^{-16}	—	[26]
16	$1^1S + 4^3P \rightarrow He_2^+ + e^-$	3.14×10^{-17}	—	[26]
17	$1^1S + 4^3D \rightarrow He_2^+ + e^-$	3.40×10^{-16}	—	[26]
	Molecular ion creation			
18	$He^+ + 1^1S + 1^1S \rightarrow He_2^+ + 1^1S$	1.40×10^{-43}	—	[26, 29]
	Excimer creation			
19	$1^1S + 1^1S + 2^3P \rightarrow He_2^* + 1^1S$	1.60×10^{-44}	—	[29]
20	$1^1S + 1^1S + 2^3S \rightarrow He_2^* + 1^1S$	1.50×10^{-46}	—	[29]
	Recombination			
21	$He^+ + e^- + e^- \rightarrow 2^1P + e^-$	5.09×10^{-37}	—	[29, 30]
22	$He^+ + e^- + e^- \rightarrow 2^3P + e^-$	1.50×10^{-38}	—	[29, 30]
23	$He^+ + e^- + e^- \rightarrow 2^1S + e^-$	1.60×10^{-37}	—	[29, 30]
24	$He^+ + e^- + e^- \rightarrow 2^3S + e^-$	5.09×10^{-37}	—	[29, 30]
25	$He_2^+ + e^- \rightarrow 2^3S + 1^1S$	1.29×10^{-16}	—	[29, 26]
26	$He_2^+ + e^- + 1^1S \rightarrow 2^1P + 1^1S + 1^1S$	1.68×10^{-42}	—	[29, 30]
27	$He_2^+ + e^- + 1^1S \rightarrow 2^3P + 1^1S + 1^1S$	5.00×10^{-42}	—	[29, 30]
28	$He_2^+ + e^- + e^- \rightarrow He_2^* + e^-$	1.34×10^{-38}	—	[29, 30]
29	$He_2^+ + e^- + e^- \rightarrow 2^3S + 1^1S + e^-$	4.47×10^{-39}	—	[29, 30]
	Quenching			
30	$1^1S + 1^1S + 2^1P \rightarrow 1^1S + 1^1S + 1^1S$	1.80×10^{-43}	—	[29, 30]
31^a	$1^1S + 3^1S \rightarrow 1^1S + 1^1S$	4.79×10^{-17}	—	[27]
32^a	$1^1S + 3^1P \rightarrow 1^1S + 1^1S$	3.53×10^{-16}	—	[27]
33^a	$1^1S + 3^1D \rightarrow 1^1S + 1^1S$	3.15×10^{-16}	—	[27]
34^a	$1^1S + 3^3S \rightarrow 1^1S + 1^1S$	3.78×10^{-18}	—	[27]
35^a	$1^1S + 3^3P \rightarrow 1^1S + 1^1S$	6.93×10^{-17}	—	[27]
36^a	$1^1S + 3^3D \rightarrow 1^1S + 1^1S$	4.54×10^{-17}	—	[27]
37^a	$1^1S + 4^1S \rightarrow 1^1S + 1^1S$	4.60×10^{-16}	—	[28]
38^a	$1^1S + 4^1P \rightarrow 1^1S + 1^1S$	7.93×10^{-16}	—	[28]
39^a	$1^1S + 4^1D \rightarrow 1^1S + 1^1S$	9.70×10^{-16}	—	[28]
40^a	$1^1S + 4^3S \rightarrow 1^1S + 1^1S$	3.02×10^{-16}	—	[28]
41^a	$1^1S + 4^3P \rightarrow 1^1S + 1^1S$	4.54×10^{-16}	—	[28]
42^a	$1^1S + 4^3D \rightarrow 1^1S + 1^1S$	5.67×10^{-16}	—	[28]
	Spontaneous Emission			
43	$He_2^* \rightarrow 1^1S + 1^1S + h\nu$ (18.41 eV)	10^9	—	[31]
44^b	$n^s l \rightarrow n'^{s'} l'$	variable	—	[32]

[a] Energy gain or loss in this reaction is ignored.

[b] n is the principal quantum number with $n > n'$, s, s' the total electron spin, and l, l' the total electron angular momentum.

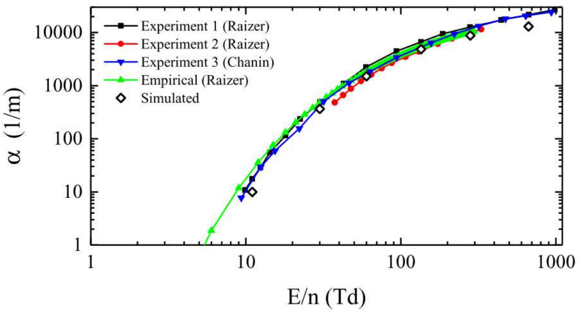

Figure 4. Calculated Townsend's first ionization coefficient (α) as a function of E/n for the given electron-neutral interaction set compared with experimental results. References are from Raizer [37] and Chanin [38].

range from approximately 10 Td to 1000 Td. Clear agreement between the experimental data [37, 38], the empirical formula [37], and the simulation is shown.

Two-body and three-body effects that either have no binary cross section available or cannot by described by a cross section are included in this model with rates from various sources (see Table 2 for included reactions). In this model, rates that depend on the temperature of the electrons or gas are included as a fixed rate with a 1 eV electron temperature and gas temperature of 300 K. The 1 eV electron temperature was determined from a series of numerical experiments and analyzing the electron energy distribution function at the point where voltage begins to collapse (t = 110 ns) and when the voltage is fully collapsed (t = 180 ns). At t = 110 ns, the temperature of the plasma bulk (defined as the region between 1 mm < x < 4 mm) is approximately 2 eV. When the voltage collapses, the temperature cools in the plasma bulk to approximately 0.7 eV. As such, a nominal temperature of 1 eV was chosen.

Self-absorption of the resonance ground transitions (2^1P → 1^1S, 3^1P → 1^1S, and 4^1P → 1^1S) were also included. The absorption cross sections were assumed to be proportional to the emission profile at a pressure of 75 torr (see [18] for details).

Neutral helium gas at a temperature of 300 K is seeded into the simulation at a pressure of 75 torr. An initial electron density of 5×10^{14} m^{-3} is also laid into the simulation uniformly within a region of 100 micron near the cathode and is justified by the application of the UV lamp in the experiment. Ions are uniformly placed throughout the entire domain with a density of 10^{13} m^{-3}. These initial ions have little effect on the transient behavior as a much higher ion density is generated via the initial electron avalanche. A timestep of 1.0×10^{-15} s is used for electric field updates and particle/photon pushing. A spatial resolution of 5 μm was used for the one-dimensional spatial domain. Simulations with a smaller mesh size yielded nearly identical results. For electrons hitting the anode, a charge accumulator variable is used and averaged over 2000 timesteps (2 ps) to obtain the discharge current.

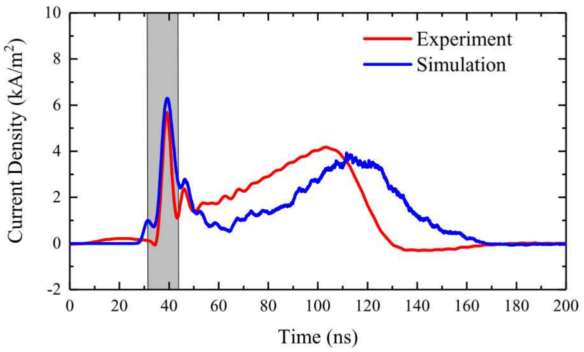

Figure 5. Comparison between current density observed in the experiment and simulation. The grey box area indicates the region where emission spectra were captured and compared between experiment and the simulation. The experimental current density assumes an electrode conduction radius of 0.7 cm.

4. Results

To synchronize in time and accurately compare the spectra from the experiment and simulation, it was necessary to also compare experimental and observed current densities. A handful of simulations were run for ion and photon secondary yields between 0.01 and 0.2. An optimal solution from these simulations was found in the simulated current by assuming a photon induced secondary emission yield, γ_{ph}, of 0.01 and ion-induced secondary emission yield, γ_{ion}, of 0.1. The numbers chosen for the simulation are within the reasonable range for both the photon and ion induced secondary yields and the influence of these coefficients will be discussed.

The comparison between simulated and experimental current density is shown in Figure 5 assuming a conduction electrode radius of 0.7 cm for the experiment. It is clear that the simulation reproduces the features in the experimental discharge current. Modifying the assumed conduction electrode radius for the experiment shifts the current density for the experiment, but will keep the same current shape. Early in the discharge, a large spike is observed in the current which is partially due to the initially seeded electrons in the domain. As will be shown later, this initial current spike may also be controlled by modifying the photon secondary emission yield. For example, if the photon secondary emission yield is reduced, this spike decreases in amplitude. After this initial current rise, a period of time elapses where more ions and electrons are generated that cause secondary emission from the cathode that leads to a more gradual increase in cur-

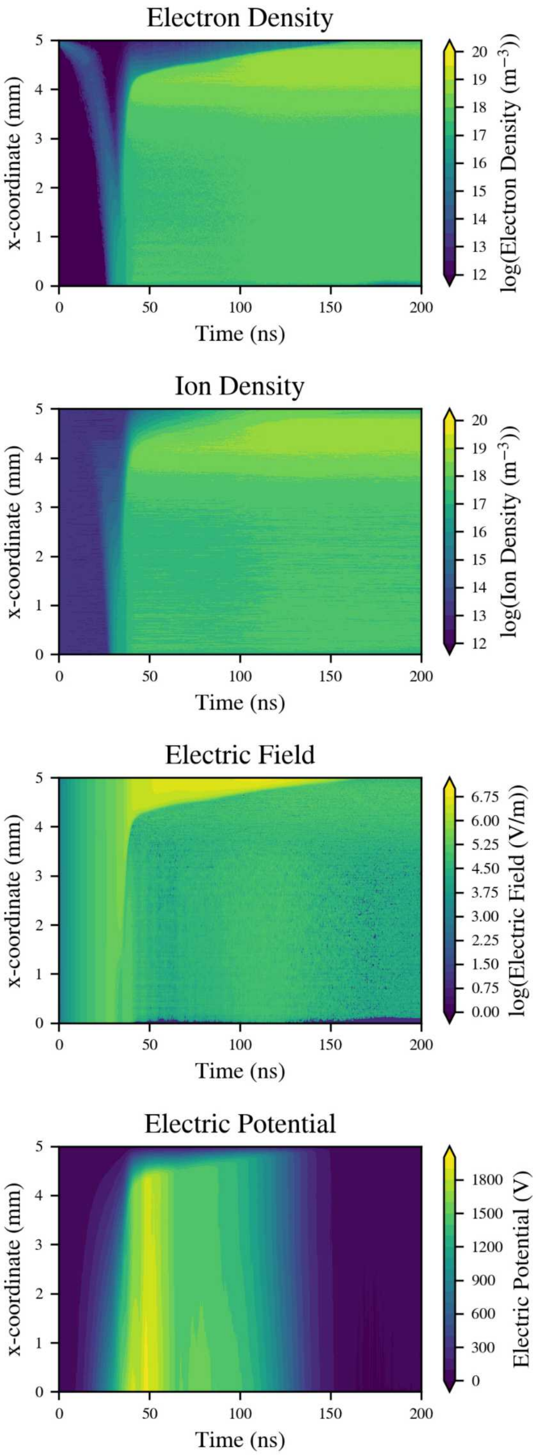

Figure 6. Log contour plot of electron and ion density plots (specified in m^{-3}) along with the electric field (specified in V/m) as a function of time and space for the conditions of $\gamma_{ph} = 0.01$, $\gamma_{ion} = 0.1$. The cathode is located at x = 5 mm and anode at x = 0 mm.

rent. This is further elucidated by examining the time and spatially-resolved electron and ion densities (Figure 6). The electrons are clearly seen starting at the cathode (x = 5 mm) and accelerating in an uniform electric field and colliding with the background helium. They finally reach the anode at approximately 30 ns leaving behind ions. At approximately 30 ns to 40 ns, the electric field transitions from being uniform across the gap to being large in magnitude near the cathode. This process is indicative of ion sheath formation.

The comparison of time-resolved emission spectra in the range between 300 nm and 700 nm is shown in Figure 7. The time window for spectra selection was set such that the current density was approximately the same in both simulation and experiment (see the grey box in Figure 5). Spatially, both spectra depicted in Figure 7 are taken from near the cathode. In the simulation, this corresponds to all photons in the region 3.5 mm < x < 4.5 mm. As mentioned previously, this work is mainly concerned with line intensities rather than shapes as the experimental apparatus has a FWHM much larger than that of the broadening mechanisms included in the model. The normalization is chosen to be the maximum of the 3^1D state at 667 nm. This is because it is not a resonance line (e.g., the 3^1P state) and has less quoted error than the spin-forbidden transitions (e.g., the 3^3D state). Notable emission lines predicted from the simulation in this region are at 501 nm, 587 nm, and 667 nm. For the most part, the simulation agrees well with the modified excitation cross sections noted in Table 1. However, the 587 nm, 492 nm, and 389 nm emission lines exhibit some error. The 587 nm and 389 nm emission line specifically emanate from a triplet state where the electron-impact excitation cross section was modified by a factor 0.3. In this case, it does not correct enough for the 389 nm emission line and overcorrects for the 587 nm emission line. For the 492 emission line that originates from a singlet state, the excitation cross section was modified by a factor 1.3. This state reportedly has the least amount of error in the calculation. The transition rates for the states are reported with less than 1% error [32]. This implies a discrepancy between the simulation and experiment that could be from the excitation cross section, the plasma chemistry model, or other parameters.

In the spectral region surveyed, the intensity of the 3^1P to 2^1S transition centered at 501 nm is sensitive to this self-absorption mechanism. Without this self-absorption included in the kinetics, the intensity of this line would exhibit further error in addition to excitation cross sections and other sources of error present in the simulation. For example, in emission spectra codes that assume local thermodynamic equilibrium (LTE) [19], and the intensity of emission lines at wavelength, λ, are proportional to

$$I(\lambda) \propto e^{\frac{-E}{k_b T}}, \tag{3}$$

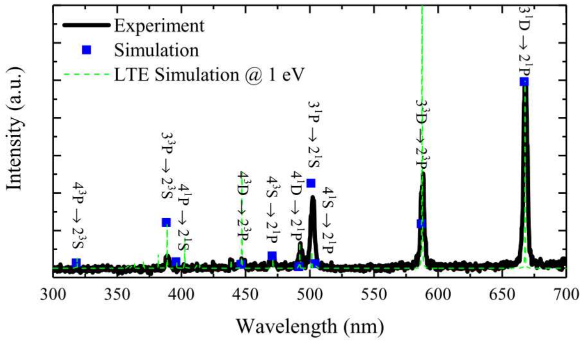

Figure 7. Comparison between spectra captured in the experiment and simulation.

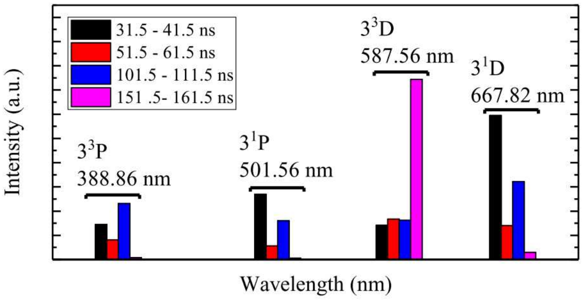

Figure 8. Simulated emission spectra as the discharge progresses. Each group of vertical bars is for the single wavelength indicated.

where E is the energy of the upper state of the transition, k_b is Boltzmann's constant, and T is the assumed temperature of the excited state distribution. Using this assumption with a temperature of 1 eV gives the emission spectra indicated in Figure 7 by the green, dashed line. The emission spectra is normalized again to the 667 nm line. It is clear that this LTE emission spectra does not agree nearly as well as the kinetic simulation. The line ratio technique has been shown to be an effective way to measure electron temperature in a helium plasma [39, 40] under the assumption of LTE. It is known that some emission lines are better for this method than others due to the re-absorption of resonance and metastable transitions. This process specifically for the 3^1P state in helium is described by first, the emission of a photon with wavelength, $\lambda = 53.7$ nm,

$$\mathrm{He}(3^1\mathrm{P}) \to \mathrm{He}(1^1\mathrm{S}) + \lambda \tag{4}$$

and the re-absorption of the same photon

$$\mathrm{He}(1^1\mathrm{S}) + \lambda \to \mathrm{He}(3^1\mathrm{P}), \tag{5}$$

which leads a modification in the decay rate of the 3^1P level. As a result, emission lines originating from the 3^1P level are affected by this emission and re-absorption process. Specifically, in Figure 7 this includes the 501 nm emission line. Overall, the discrete photon approach demonstrates the ability to calculate, *in situ*, non-equilibrium emission spectra.

Figure 8 depicts the simulated emission spectra of the four most intense emission lines in this region for various times throughout the discharge process. For the 388 nm and 667 nm emission lines, the intensity follows the general trend of being the brightest at the beginning of the discharge, followed by a decrease in intensity. As the voltage collapses to zero, the intensity of these lines once again increases. To observe this effect in greater detail, the intensity of the emission lines in the 350 nm to 700 nm region are shown as a function of time in Figure 9. As the voltage rises the intensity of the emission responds proportionally. At about 50 ns, the intensity of all emission lines slightly decreases. A sharp increase in intensity can be seen for the 396 nm, 447 nm, 501 nm, 587 nm emission lines at about 110 ns. The 587 nm emission line experiences a large intensity increase and decays slower in intensity relative to other emission observed. The slower intensity decay is likely due to the order of magnitude smaller quenching coefficient for the upper state (3^3D) as compared to, for example, the 667 nm emission line upper state (3^1D).

5. Discussion

There are clear uncertainties in the photon and ion induced secondary emission yield. For example, it has been shown that as the energy of photons approaches 10 eV, the photon induced secondary emission coefficient may approach 0.01 to 0.1 for some metals [37]. Furthermore, the apparent work function of metals has been shown to change under exposure to air [41]. While radiation transport has been included in low-temperature plasma discharge

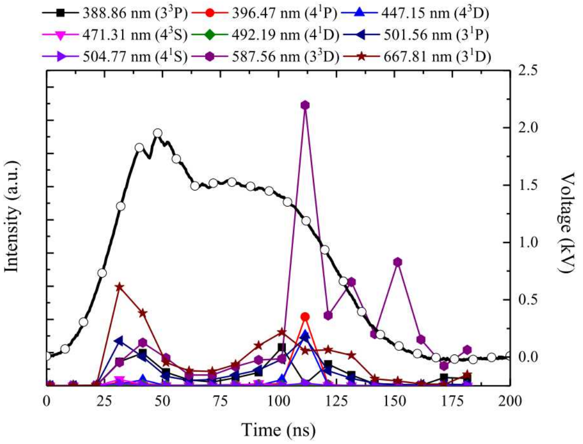

Figure 9. Emission intensities for atomic helium emission lines between 350 and 700 nm as a function of time. The solid black line with open circles indicates the applied voltage over time.

models, these investigations have mainly focused on photoionization in streamer formation (e.g. [42, 43]). With the incorporation of the discrete photon approach, investigation of photon-surface effects is possible while including self-absorption effects. In this work, photoemission from the cathode may be induced due to photons from both atomic resonance and excimer emission. Excimer emission is a three-step process. First an excited state of atomic helium must be created, then it must interact with background neutrals, and finally emit a photon. Resonance atomic emission, on the other hand, is only a two-step process generated via creation of an excited state and subsequent photon emission. The inclusion of both of these mechanisms is to supplement studies that have focused on either purely excimer emission [44, 45] or purely atomic resonance emission [46, 18].

Figure 10 shows the effect of both the atomic resonance and excimer emission in regards to injected electron current at the cathode due to photon impact. Two cases are shown for both $\gamma_{ph} = 0.01$ and $\gamma_{ph} = 0.2$. Although highly self-absorbed, the resonance emission still dominates in the production of new electrons at the cathode surface. For both cases the current generated from resonance emission is approximately 50 times higher than that of the excimer emission.

Various different photon induced secondary emission coefficients were also investigated to observe their effect on the discharge current. The effect of increasing the coefficient from 0.01 to 0.20 is shown in Figure 11. The initial current spike is increased as the photon induced secondary emission coefficient is increased. After t = 50 ns, the slope of the current increases also as γ_{ph} is increased.

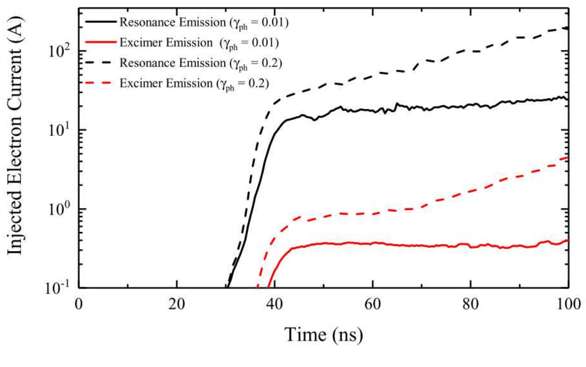

Figure 10. Electron current generated from the cathode from atomic resonance emission (52.2 nm, 53.7 nm, and 58.4 nm) and from excimer emission (67.4 nm) for the first 100 ns of the discharge. The solid lines indicate the simulation where γ_{ph} = 0.01, the dashed lines are for γ_{ph} = 0.2. In both cases, γ_{ion} = 0.1.

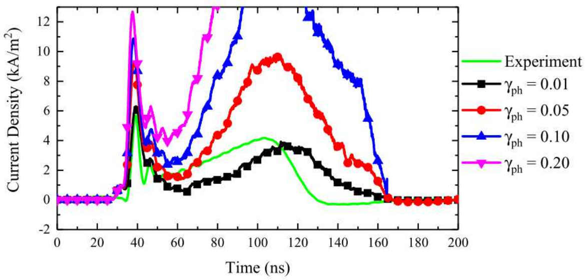

Figure 11. Simulated discharge current densities for the different photon induced secondary yield coefficients indicated. The green solid line (no symbols) shows the experimental current density. In all cases, γ_{ion} = 0.1. Note: the black squares (γ_{ph} = 0.01, γ_{ion} = 0.1) is the same curve as in Figure 12.

For ion induced secondary emission, a classical empirical approximation for the yield coefficient is given by [37, 47],

$$\gamma_{ion} \approx 0.016(\mathrm{W}_{iz} - 2\phi) \tag{6}$$

where W_{iz} is the ionization potential of the impacting ion and ϕ is the work function of the cathode material. The helium ion impacting an aluminum electrode in this case should yield a secondary emission coefficient of approximately ∼0.25. Other works have used coefficients of 0.3 for helium ions on aluminum depending on operating conditions [9], 0.15 for helium ions [46], and 0.1 for ions on a dielectric surface [48]. Depending on surface preparation, air contaminants, and background conditions, the same surface may exhibit vastly different secondary emission properties [49].

In this work, an ion induced secondary yield coefficient of $\gamma_{ion} = 0.1$ was used for all impacting ion energies. The resulting simulated current density for varying this coefficient is shown in Figure 12. Similar to increasing the photon induced secondary yield coefficient, after t = 50 ns, the slope of the current increases with increasing γ_{ion}. However, it is clearly seen that modifying the secondary yield coefficient does little to impact the initial current spike. This indicates that the magnitude of this initial current spike is controlled by the photon induced secondary yield coefficient. Based on these results, the optimal solution chosen was with $\gamma_{ion} = 0.1$ and $\gamma_{ph} = 0.01$.

Another region of uncertainty is the use of fixed rate coefficients for the reactions indicated in Table 2. A fixed temperature of 1 eV was assumed for the electrons. The reaction rates vary greatly with electron temperature and as a result is the most likely source of error as the gas temperature is not expected to increase on these short time scales. Future research will include temperature dependent rates to study their impact on this particular problem. It is expected that as the electron temperature cools rapidly at the end of the pulse, recombination coefficients would increase as they are inversely proportional to electron temperature [29].

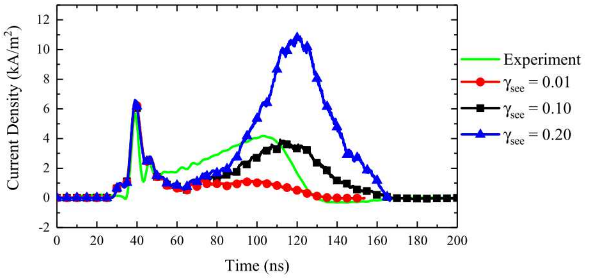

Figure 12. Simulated discharge current densities for the different ion induced secondary yield coefficients indicated. The green solid line (no symbols) shows the experimental current density. In all cases, γ_{ph} = 0.01. Note: the black squares (γ_{ph} = 0.01, γ_{ion} = 0.1 is the same curve as in Figure 11.

6. Conclusion

An experiment has been constructed that is contains planar aluminum electrodes separated by 0.5 cm in pure helium gas. To generate a plasma under non-equilibrium conditions, a transient voltage pulse was applied and evaluated with electrical diagnostics and spectroscopic techniques. The experimental data was used and compared to a simulation of the same physical setup. The data gathered from OES were relatively calibrated with a known white light source.

A recently developed photon model incorporated into the Aleph code was employed to validate the underlying physics of a one-dimensional discharge simulation to that of the experiment. Synthesized emission spectra captured with the same integration window as that of the ICCD camera were compared to the experimental results with normalizations. The experimental and simulated discharge currents show the same type of discharge features of a fast, initial current spike followed by a slow rise in current when the voltage is somewhat steady. Comparison of the spectra between simulation and experiment indicates the ability for the radiation transport method to simulate non-LTE emission spectra that in some cases, such as this one, agrees better with experiment.

Acknowledgments

This work was supported by the Department of Energy Office of Fusion Energy Sciences at the U.S. Department of Energy under contract No. DE-AC04-94SL85000. Additional support was provided by Sandia National Laboratories Laboratory Directed Research and Development (LDRD) program under project 209241. Sandia National Laboratories is a multimission laboratory managed and operated by National Technology & Engineering Solutions of Sandia, LLC, a wholly owned subsidiary of Honeywell International Inc., for the U.S. Department of Energys National Nuclear Security Administration under contract DE-NA0003525.

References

[1] Turner M M and Vukovic M 2012 *Workshop on Verification and Validation of Computers Simulations in Low Temperature Plasma Physics* (Gaseous Electronics Conference)
[2] Fierro A, Stephens J, Beeson S, Dickens J and Neuber A 2016 *Phys. Plasmas* **23** 013506
[3] Turner M M 2016 *Plasma Sources Sci. Technol.* **25** 054007
[4] Schregel C, Carbone E, Luggenholscher D and Czarnetzki U 2016 *Plasma Sources Sci. Technol.* **25** 054003
[5] Carbone E, Schregel C and Czarnetzki U 2016 *Plasma Sources Sci. Technol.* **25** 054004
[6] Turner M M, Derzsi A, Donko Z, Eremin D, Kelly S, Lafleur T and Mussenbrock T 2013 *Phys. Plasmas* **20** 013507
[7] Surendra M 1995 *Plasma Sources Sci. Technol.* **4** 56–73
[8] Bagheri B, Teunissen J, Ebert U, Becker M, Chen S, Ducasse O, Eichwald O, Loffhagen D, Luque A and Mihailova D 2018 *Plasma Sources Sci. Technol.* **27** 095002
[9] Carlsson J, Khrabrov A, Kaganovich I, Sommerer T and Keating D 2017 *Plasma Sources Sci. Technol.* **26** 014003
[10] Hopkins M M, Crozier P and Moore C 2014 Comparison of Aleph and BOLSIG+ Results for Electron-Nitrogen Chemistry Tech. rep. Sandia National Laboratories, SAND2014-19653
[11] Radtke G, Musson L and Cartwright K 2012 Error estimation for Aleph PIC plasma sheath simulations Tech. rep. Sandia National Laboratories, SAND2012-5195C
[12] Roark C and Stoltz P 2012 Aleph Verification Simulations Tech. rep. Sandia National Laboratories, SAND2012-5192C
[13] Crozier P and Stewart P 2010 Arc simulations with Aleph Tech. rep. Sandia National Laboratories, SAND2010-6564C
[14] Bettencourt M 2015 Aleph code electrostatic solver verification Tech. rep. Sandia National Laboratories, SAND2015-0339
[15] Hooper R and Moore S 2015 Aleph field solver challege problem results summary Tech. rep. Sandia National Laboratories, SAND2015-0317
[16] Boerner J, Pacheco J and Grillet A 2016 Evaluation of the Aleph PIC Code on Benchmark Simulations (Gaseous Electronics Conference)
[17] Timko H, Crozier P, Hopkins M M, Matyash K and Schneider R 2012 *Contr. to Plasma Phys.* **52** 295–308
[18] Fierro A, Moore C, Scheiner B, Yee B and Hopkins M M 2017 *J. Phys. D: Appl. Phys.* **50** 065202
[19] Fierro A, Laity G and Neuber A 2012 *J. Phys. D: Appl. Phys.* **45** 495202
[20] Bruggeman P, Sadeghi N, Schram D and Linss V 2014 *Plasma Sources Sci. Technol.* **23** 023001
[21] van der Horst R, Verreycken T, van Veldhuizen E and Bruggeman P 2012 *J. Phys. D: Appl. Phys.* **45** 345201
[22] Birdsall C and Langdon A 2005 *Plasma Physics via Computer Simulation* (McGraw-Hill)

[23] Bird G 1994 *Molecular Gas Dynamics and the Direct Simulation of Gas Flows* (Oxford University Press)

[24] Fierro A, Moore C, Yee B and Hopkins M 2018 *Plasma Sources Sci. Technol.* **27** 105008

[25] Surendra M, Graves D and Jellum G 1990 *Phys. Rev. A* **41** 1112–1125

[26] Alves L, Gousset G and Ferreira C 1992 *J. Phys. D: Appl. Phys.* **25** 1713–1732

[27] Dubreuil B and Catherinot A 1980 *Phys. Rev. A* **21** 188–199

[28] Catherinot A and Dubreuil B 1981 *Phys. Rev. A* **23** 763–774

[29] Belmonte T, Cardoso R, Henrion G and Kosior F 2007 *J. Phys. D: Appl. Phys.* **40** 7343–7356

[30] Emmert F, Angermann H, Dux R and Langhoff H 1988 *J. Phys. D: Appl. Phys.* **21** 667–674

[31] Golubovskii Y, Maiorov V, Behnke J and Behnke J 2003 *J. Phys. D: Appl. Phys.* **36** 39–49

[32] A Kramida and Y Ralchenko and J Reader and NIST ASD Team NIST Atomic Spectra Database (ver. 5.3), [Online]. Available: http://physics.nist.gov/asd [2016, March 3]. National Institute of Standards and Technology, Gaithersburg, MD

[33] Yee B, Scheiner B, Baalrud S, Barnat E and Hopkins M 2017 *Plasma Sources Sci. Technol.* **26** 025009

[34] Scheiner B, Barnat E, Baalrud S, Hopkins M and Yee B 2018 *Phys. Plasmas* **25** 043513

[35] S Biagi Biagi Database, www.lxcat.net, retrieved on July 30, 2018.

[36] Ralchenko Y, Janev R, Kato T, Fursa D, Bray I and Heer F 2008 *Atomic Data and Nuclear Data Tables* **94** 603–622

[37] Raizer Y 1997 *Gas Discharge Physics* (Springer)

[38] Chanin L 1964 *Phys. Rev.* **133** 1005

[39] Lee W, Park K, Kwon D and Oh C 2016 *Phys. Plasmas* **23** 063516

[40] Podder N, Johnson J, Raynor C, Loch S, Ballance C and Pindzola M 2004 *Phys. Plasmas* **11** 5436

[41] Berg M, Bussman E, Smith S, Scrymgeour D, Ohta T, Hjalmarson H, Schultz P, Clem P, Hopkins M and Moore C 2018 Characterizing the influence of electrode surface morphology on field emission (Mechanisms of Vacuum Arcs)

[42] Bourdon A, Pasko V, Liu N, Celsetin S, Segur P and Marode E 2007 *Plasma Sources Sci. Technol.* **16** 656

[43] Kulikovsky A 2000 *J. Phys. D: Appl. Phys.* **33** 1514

[44] Bourdon A, Darny T, Pechereau F, Pouvesle J, Viegas P, Iseni S and Robert E 2016 *Plasma Sources Sci. Technol.* **25** 035002

[45] Naidis G 2010 *J. Phys. D: Appl. Phys.* **43** 402001

[46] Donko Z, Hamaguchi S and Gans T 2018 *Plasma Sources Sci. Technol.* **27** 054001

[47] Lieberman M and Lichtenberg A 2005 *Principles of Plasma Discharges and Materials Processing* (John Wiley and Sons)

[48] Jansky J and Bourdon A 2014 *Plasma Sources Sci. Technol.* **23** 025001

[49] Phelps A and Petrovic Z 1999 *Plasma Sources Sci. Technol.* **8** R21–R44